Simulations and linear stability analysis of vortex shedding angle in solid rocket motors

Laura Lacassagne[⋆], Franck Godfroy[⋆] and Glen Sire[†]
[⋆]*ArianeGroup*
[†]*Alten*
ArianeGroup (CRB), 91710 Vert-le-Petit, France
laura.lacassagne@ariane.group · franck.godfroy@ariane.group · glen.sire@alten.com

Abstract

The vortex shedding angle is studied in P80 (1st stage of VEGA launcher) and P120C motors (1st stage of Ariane 6 and VEGAC launchers) with linear stability analysis. This hydrodynamic phenomenon, first investigated by Dupays[7,8] has been recently reviewed by Lacassagne[19] from an academic point of view. Based on the method and tool used is this academic work, this study enables to demonstrate that, at the selected operating times, the risk of triggering vortex shedding angle in the P80 and P120C is negligible. Therefore, pressure oscillations measured in this part of the firing must be explained by another instability source.

1. Introduction

Pressure oscillations are a major issue in solid rocket motors (SRM) dedicated for spatial missions and designing motors that produce as small pressure oscillations as possible represents an important industrial challenge. One possible source of pressure oscillations is hydrodynamic instabilities[28] and can be due to the motors length (VSP)[3,14,15] , can be created by an obstacle in the geometry (VSO)[9,21,26] or by a geometry section changes (VSA)[7,8,19] . In the current motors designs, the order of importance of theses instabilities is slightly modified and the vortex shedding angle (VSA), let logically aside in the past, becomes today one of the most likely source of hydrodynamic instability. This instability appears when geometry exhibits a propellant tapered edge, generating strong shear flows in the cross-stream direction. Shear flows are known to be prone to instabilities since temporally or spatially growing waves are generated along the stream and lead to the formations of unsteady vortical structures.

In the past 50 years, stability of the shear layer has been continuously studied and classical theory is nowadays well known[6,16] . However, because of the sidewall injections, from the solid propellant burning, velocity profiles generated in the shear layer are quite different from the one of a classical hyperbolic tangent mixing layer[22,23] . Recent studies[19,20] have shown that this difference has in fact a strong impact on the stability of the shear layer, very sensitive to the lateral blowing. However, only academic configurations have been studied.

This work aims to apply linear stability analysis to real motor geometries, namely the P80 (1st stage of VEGA launcher) and P120C motors (1st stage of Ariane 6 and VEGAC launchers), where the propellant exhibits section changes. This study is being carried out in the context of the P120C development and it is part of the AGS strategy defined by a continually improving of our knowledge and control of pressure oscillations. The P80 motor has been largely studied in the VEGA developments[4,10,24] . Thanks to this knowledges and due to similar geometry, P80 study aims to reinforce P120C results.

Moreover, the physical explanations of specific bursts of these motors are still debated. A way to explain some of these bursts, occurring in the last part of the first half of operating time, can eventually be linked to shear layer instability, even if our CFD simulations do not exhibit this kind of phenomena. The linear stability analysis performed in this study enable to bring answers without additional costly CFD simulations.

This paper is organized into three main parts. In the first part, the P80 and P120C solid rocket motors are presented. The similarities between both geometries are highlighted and the analysed cases are defined. In the second part, after a quick recall on linear stability theory, the main results of previous academic work[19] are presented. The last part of this paper is dedicated to the P80 and P120C applications. The analysis if first carried out for the P80 motor and then compared to the one performed for the P120C motor.

2. Presentation of the P80 and P120C motors

As presented in Figure 1, P80 and P120C geometries are very similar. It is then largely justified to first analysed the P80, witch is the most studied and well-known motor and then applied the same kind of analysis on the newer P120C. For each motors, four geometries are considered, named OT1, OT2, OT3 and OT4. Each geometry corresponds to a specific operating time, located in Figure 2 and Figure 3 on the mean head-end pressure evolutions.
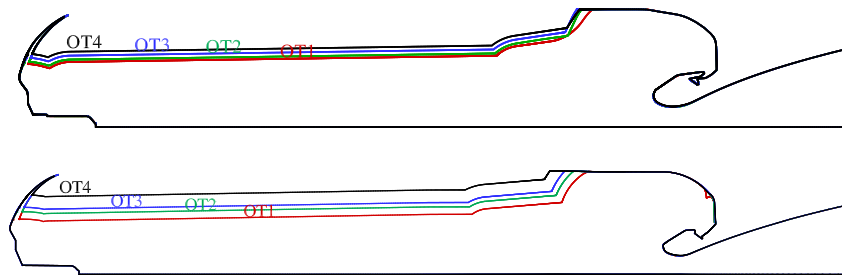
Figure 1: P80 (up) and P120C (down) geometries for all operating points.

Let's focus first on the P80 configuration. As shown in Figure 2, by collecting pressure oscillation measures on static firing tests (DM and QM) and VEGA flights (VV01, VV02 and VV03) four different bursts are clearly present: namely B0, B1, B2 and B3. For B0 and B1, the scenario is well established. The first burst B0 is due to a hydrodynamic instability namely the parietal vortex shedding instability, while the triggering mechanism of the second one B1 is more "hybrid" with the combination of the parietal vortex shedding and the aluminium combustion instability called ITHAC[11–13] . However the physical explanations of the B2 and B3 bursts are not so obvious.

First, theory and simulation show that the parietal vortex shedding is not present in this second part of the firing. Then, AGS studies demonstrate that the driving phenomenon is the aluminium combustion which leads to the modulation of pressure oscillation levels. However, vortex shedding angle instability must not be discarded and could represent a significant source of instability if the shear layer due to the section changes at the back-end of the motor is unstable.
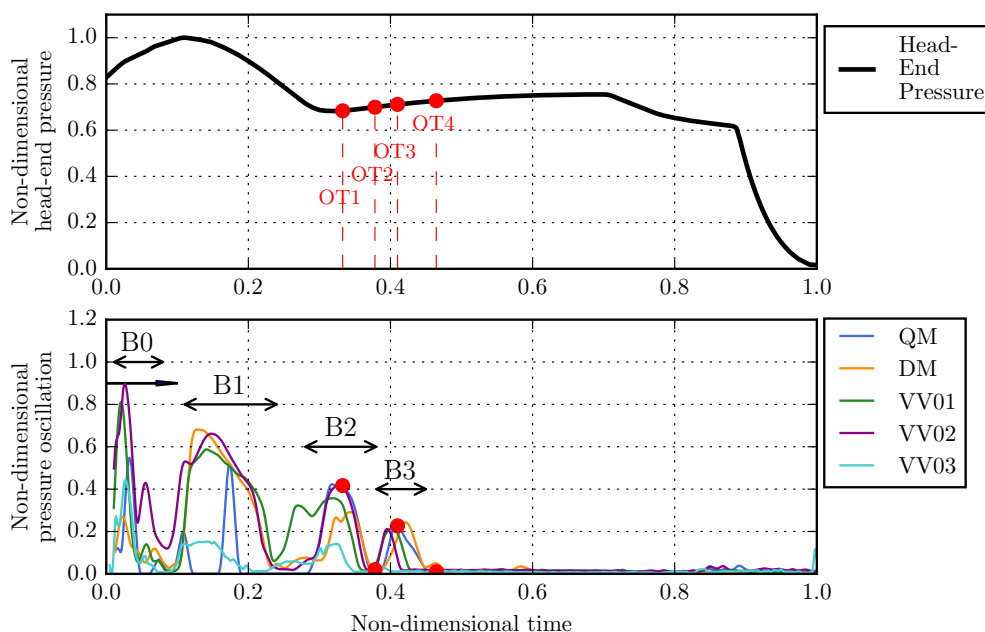
Figure 2: P80 head-end pressure evolution and pressure oscillations measured during firing tests (DM and QM) and VEGA flights (VV01, VV02, VV03). The studied cases (OT1, OT2, OT3 and OT4) are located with red symbols.

To bring answer to this question, as shown in Figure 2, the OT1 and OT3 cases are chosen to be at the maximum of pressure oscillations of burst B2 and B3 respectively, OT2 at the cross-bursts and OT4 after burst B3. Then, the com-
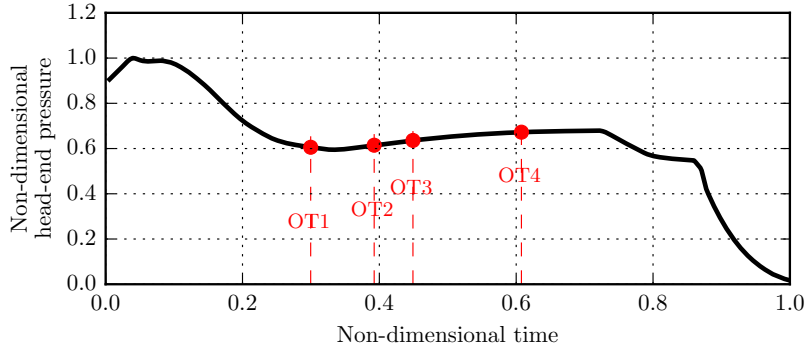
Figure 3: P120C head-end pressure evolution. The studied cases (OT1, OT2, OT3 and OT4) are located with red symbols.

parison of the linear stability analysis on this four operating times will enable to evaluate if the shear layer instability is the triggering mechanisms of these bursts.

In the same way, for the P120C, the four cases are chosen in the second part of the firing before the pressure decreases as shown in Figure 3.

As recalled in the next part, the linear stability analysis is based on mean velocity profiles. To get this information, monophasic steady state CFD simulations are performed on each cases. These simulations are cheap, cost-effective and sufficient to bring the input data of linear stability analysis.

3. Theory of linear stability analysis and academic cases

Linear stability analysis of the time-averaged flow has already been proven useful and powerful in a lot of various configurations like vortex shedding downstream a cylinder,[18] parietal vortex shedding[1,3,5] and angle vortex shedding[7,8,19,20] in solid rocket motors, as well as fuel injectors exhibiting coherent structures in swirled jets.[17,25]

A local analysis formalism is used in this work, meaning that the local stability behaviour is computed at each axial position of the flow based on local time-averaged velocity profiles at the given axial position.

3.1 The linear stability theory and numerical methods

In this approach, the Navier-Stokes equations are linearized around a steady axisymmetric base flow. Then, each quantity Q can be decomposed into a mean part $\bar{Q}$ also called the base flow and a fluctuating part q to be determined. For an axisymmetric and incompressible flow, the decomposed variables are defined by Eq. (1).

$$
\begin{aligned}
(U_x, U_r, U_\theta, P)(x, r, \theta) =& (\bar{U}_x, \bar{U}_r, \bar{U}_\theta, \bar{P})(x, r) + \\
& (u_x, u_r, u_\theta, p)(x, r, \theta, t)
\end{aligned}
\tag{1}
$$

Following the parallel flow hypothesis, the base flow is assumed to only depend on the radial coordinate r. It should be noted that this hypothesis is not fully satisfied here since the geometry and the parietal injection imposed an axial dependence of the base flow, significant at the proximity of the corner, ignored here. However this assumption has been successfully used in the stability study as well as for VSP, where good agreement between theoretical and experimental results are found[14,27], than for the VSA[7,20].

Fluctuating quantities q are formulated using normal mode decomposition given by Eq. (2).

$$
q(x, r, \theta, t) = \hat{q}(r)e^{i(\alpha x + m\theta - \omega t)}
\tag{2}
$$

In Eq. (2) $\hat{q}$ is a complex function called amplitude function, m is an integer representing the azimuthal wave number and α and ω are generally complex numbers.

In the case of a convective instability like the one expected in the present mixing layer, using a spatial analysis formalism is more relevant and is the one chosen in this work. Therefore ω is a real number and $\alpha = \alpha_r + i\alpha_i$ is a

complex value. In this work, the azimuthal wave number m is set to zero since only axisymmetric modes are studied in agreement with the axisymmetric simulations presented above. Eq. (2) can then be rewritten in Eq. (3).

$$q(x, r, \theta, t) = \hat{q}(r)e^{-\alpha_i x}e^{i(\alpha_r x - \omega t)} \tag{3}$$

In Eq. (3) the second exponential term is of norm one and describes the wavy nature of the solution for the fluctuation, α_r being the wave number and ω the circular frequency, with $f = \omega/2\pi$ being the frequency itself. The first exponential in Eq. (3) is real and reflects the amplification or the attenuation of the perturbation with the distance x according to the sign of α_i and the propagation direction of the unstable mode.

The problem now is to determine the amplitude function $\hat{q}$ as well as the frequency and complex wave number α, so that perturbations given by Eq. (3) satisfy the linearized Navier-Stokes equations and boundary conditions. These conditions constitute the dispersion relation defined by Eq. (4). Except for very simple cases, this relation cannot be analytically determined and is solved numerically.

$$\mathcal{F}(\bar{Q}, \alpha, \omega, m) = 0 \tag{4}$$

After discretization the linearized equations can be transformed into a generalized eigenvalue problem as the one expressed in Eq. (5). X, defined by Eq. (6) is a vector holding unknowns $\hat{q}_j$ at each discretization point j.

$$A.X = \alpha.B.X \tag{5}$$

$$X = \left[\hat{u}_x, \hat{u}_r, \hat{u}_\theta, \hat{p}\right] \tag{6}$$

The linearized equations are associated to boundary conditions at the wall ($r = R$, Eq. (7)) and at the axis ($r = 0$, Eq. (8) with $m = 0$).

$$\hat{u}_x(R) = \hat{u}_r(R) = \hat{u}_\theta(R) = 0 \tag{7}$$

$$\frac{d\hat{u}_x}{dr}(0) = \hat{u}_r(0) = \hat{u}_\theta(0) = 0 \tag{8}$$

Several methods can be used to solve an eigenvalue problem, but the one chosen is the spectral collocation method[2] which consists in decomposing the functions to discretize, here the amplitude functions, on a polynomial basis. The Tchebytchev polynomials are used associated to Gauss-Lobatto discretization points.[2]

To get the spatial behaviour of the mixing layer, several linear stability analysis at different axial positions are needed. Indeed, the fluctuating quantity q, defined Eq. (3), can be rewritten by Eq. (9) with $m = 0$ and $t = 0$. This expression introduces the perturbation modulus $|\hat{q}(r)|$ and phase $\varphi_{\hat{q}}(r)$ of the eigenfunction $\hat{q}(r)$. This definition also includes integrated quantities over axial positions. The first one is the phase φ_{α_r}, defined Eq. (10) and introduced by the axial wave number α_r. The second one is n, called the n-factor and defined Eq. (11) which represents the integration of $-\alpha_i$ over the axial positions, x_0 being the first position studied.

$$q(x, r, t) = |\hat{q}(r)|e^{n}e^{i(\varphi_{\alpha_r} + \varphi_{\hat{q}}(r))} \tag{9}$$

$$\varphi_{\alpha_r} = \int_{x_0}^{x} \alpha_r(\xi)d\xi \tag{10}$$

$$n = \int_{x_0}^{x} -\alpha_i(\xi)d\xi \tag{11}$$

As observed, e^n is the term that modifies the amplitude of the perturbation. Since, this work aims to study the risk of triggering instability in the shear layer, the term of interest here is e^n. To evaluate this term, the evolution of $-\alpha_i$ with the perturbation frequency f is first determined for all the axial positions. This evolution if called the dispersion curves.

SIMULATIONS AND LINEAR STABILITY ANALYSIS OF VORTEX SHEDDING ANGLE IN SOLID ROCKET MOTORS

3.2 Academic studies

Before performed the P80 and P120C analysis, it is useful to recall the main results of the academic studies performed by Lacassagne[19,20] . Indeed, in this work, several shear layers in headwall injections configurations are studied with unsteady simulations and linear stability method. The geometry used is recalled on the left hand side in Figure 4. If the injection velocity applied on the upper surface is large enough, the shear layer is stable like in the R100 case presented in Figure 4(b) and no fluctuations are measured in the shear. On the other hand, if the injection velocity is small, like in the R000 case presented in Figure 4(c), the shear layer is unstable, velocities fluctuations are measured in the shear linked to the creation of vorticity structures characteristics of vortex shedding angle instability (VSA).
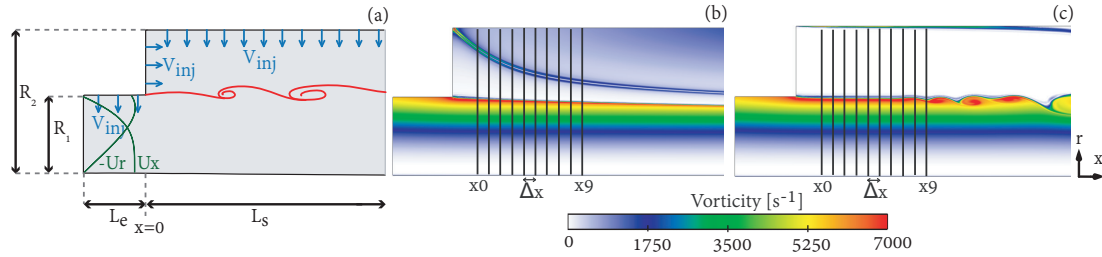
Figure 4: Schematic view of the configuration (a) and vorticity fields of a stable case (R100) (b) and of an unstable case (R000) (c). Extracted from Lacassagne.[19]

The important point here is that, even if in a stable case, as the one shown in Figure 4(b), weak positive spatial amplifications $-\alpha_i$ are found by the linear stability analysis. Indeed, as shown in Figure 5(a)(i) for the R100 case, the dispersion curves obtained at each axial position (x_0 to x_9), presents a frequency range where $-\alpha_i$ is positive meaning where perturbation is amplified. These positive spatial amplifications lead to positive n-factor and positive e^n term, as shown in Figure 5(b)(i).

However, the value of the amplification term if one order of magnitude smaller than in a real unstable case (R000). Indeed, as shown in Figure 5(b)(ii), in the unstable R000 case the maximum of the amplification term e^n is about 10 times higher than the one of the stable R100 case.

It is then important to note that, with this local approach, a positive amplification term e^n is not sufficient to affirm that the shear layer will be hydrodynamically unstable and that vorticity structures will be generated. These academic cases will be used as reference cases in order to evaluate if the P80 and P120C shear layers are enable to trigger angle vortex shedding instability.
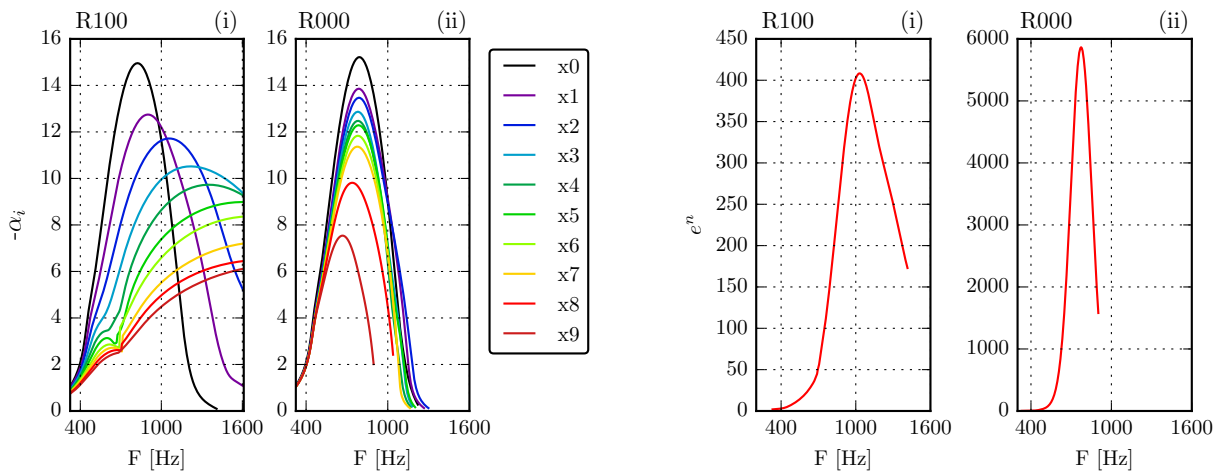
(a) Evolution of $-\alpha_i$ for each axial position (x_0 to x_9) with the frequency F of the perturbation.

(b) Evolution of e^n with the frequency F of the perturbation.

Figure 5: Linear stability analysis of the stable case R100 and the unstable case R000.

4. Application to P80 and P120C motors

As explained in the introduction, the linear stability analysis is performed on the P80 motor as a first step and then applied in the same way to the P120C.

4.1 Stability of the P80 profiles

Mean velocity profiles are extracted from steady state simulations for each geometries (OT1, OT2, OT3 and OT4) at several axial positions in the shear layer, as shown in Figure 6.
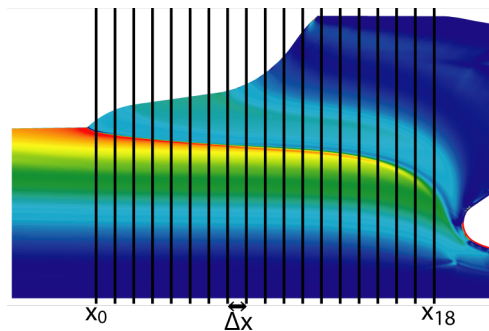
Figure 6: Position on a mean vorticity field of the OT1 case, of the analysed cuts in the P80 shear layer, from x_0 to x_{18}.

The linear stability analysis gives the dispersion curves presented in Figure 7, for each axial position and for each operating time.
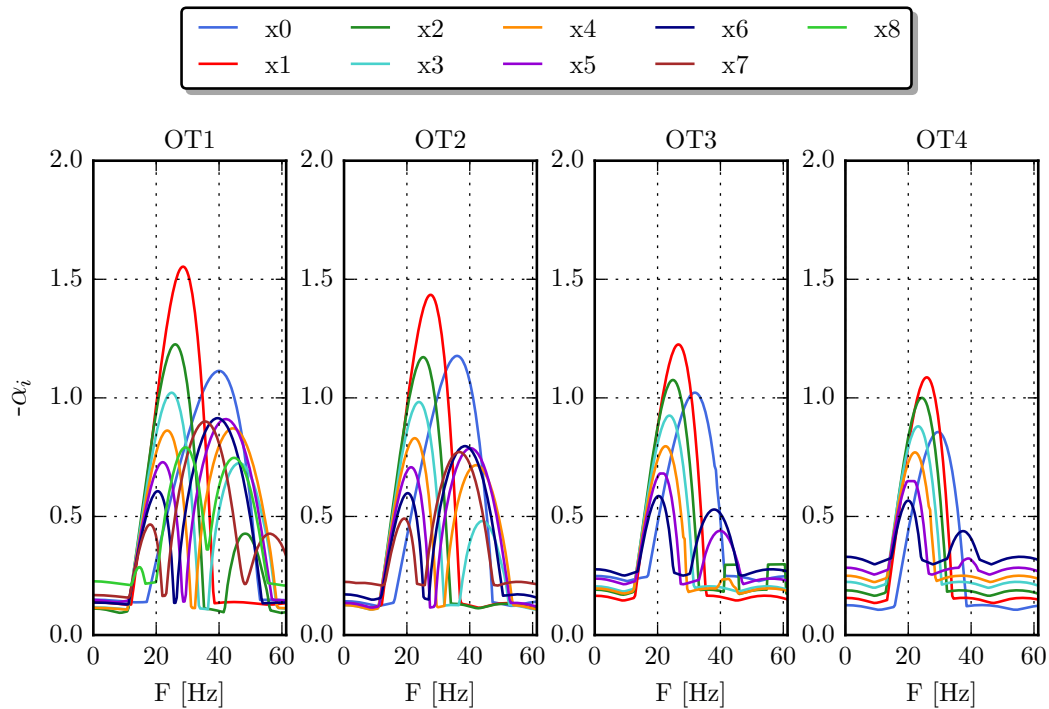
Figure 7: Linear stability analysis of the P80 at each operating times ($OT1$ to $OT4$). Evolution of the spatial amplification $-\alpha_i$ for each axial position from $x0$ to $x9$ with the frequency F of the perturbation.

First of all, positive spatial amplification $-\alpha_i$ are obtained for all the cases but with very small levels. In the P80 shear layers, the maximum spatial amplification $-\alpha_i$ is one order of magnitude smaller and the maximum of the e^n term (cf. Figure 8) is two order of magnitude smaller than the ones of the academic stable case R100 (cf. Figure 5(a)(i) and

Figure 5(b)(i)). The shear layers in this four P80 operating times are even more stable than the stable academic shear layer.

Moreover, the maximum amplified frequency is around 25 Hz for all the cases, quite far from the first acoustic longitudinal mode witch is between 50 Hz and 60 Hz. There is even less chances of a coupling between acoustic and hydrodynamic instability.

Finally, the maximum of the amplification factor for the four cases do not follow the evolution of pressure oscillations measured. Indeed, the linear stability predict that OT1 would be the most unstable followed by OT2, then by OT3 and finally by OT4. If the shear layer instability would be the source of the bursts (cf. Figure 2), OT3 would be the second most unstable.
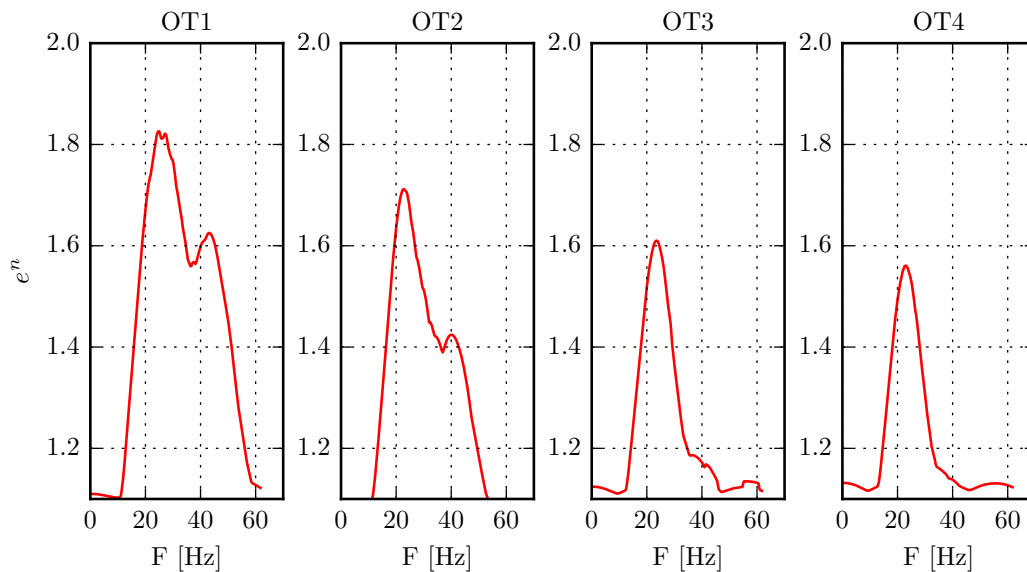
Figure 8: Linear stability analysis of the P80 at each operating times ($OT1$ to $OT4$). Evolution of e^n with the frequency F of the perturbation.

In other words, in this part of this firing, there is no risk to trigger corner vortex shedding instability and bursts B2 and B3 identified in Figure 2 can not be due to this hydrodynamic instability.

4.2 Stability of the P120C profiles

Finally the same analysis is performed on the P120C motor for the four cases defined in Figure 1 and in Figure 3. Mean velocity profiles are extracted from steady state simulations at several axial position in the shear layer located in Figure 9.
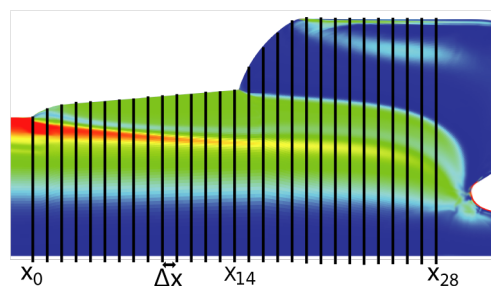
Figure 9: Position on a mean vorticity field of the OT1 case of the analysed cuts in the P120C shear layer, from x_0 to x_{28}.

SIMULATIONS AND LINEAR STABILITY ANALYSIS OF VORTEX SHEDDING ANGLE IN SOLID ROCKET MOTORS

The particularity of P120C geometry is that two distinct shear layers are generated in the flow due to two abrupt section changes. As shown in Figure 9, the first one is located around the position x_0 and the second one is located around the position x_{14}. The P80 do not exhibit the second shear layer since the geometry has a round shape at this position.

Only some of the dispersions curves are plotted in Figure 10 to keep a readable figure but all the positions are used to compute the e^n term defined in Eq. (11) and plotted in Figure 11.
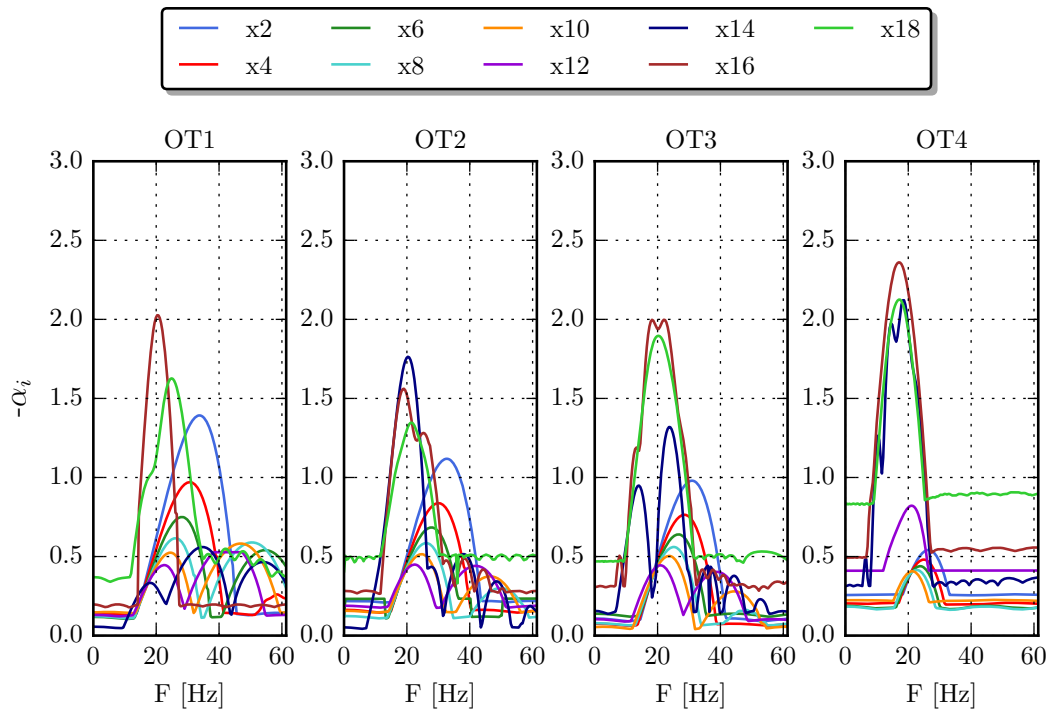
Figure 10: Linear stability analysis of the P120C at each operating times ($OT1$ to $OT4$). Evolution of the spatial amplification $-\alpha_i$ for each axial position from x_2 to x_{18} with the frequency F of the perturbation.
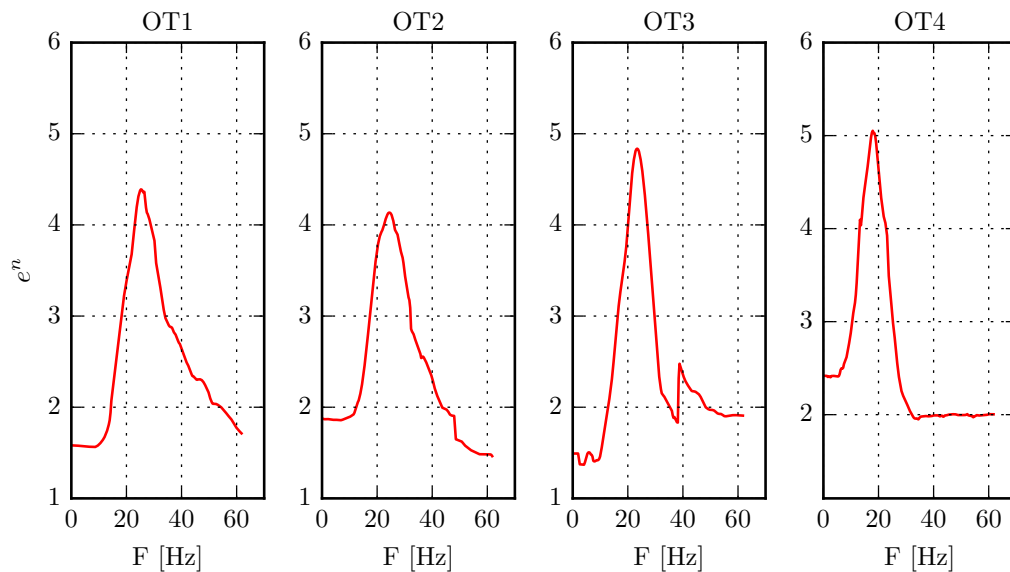
Figure 11: Linear stability analysis of the P120C at each operating times ($OT1$ to $OT4$). Evolution of e^n with the frequency F of the perturbation.

8

First of all, the two different shear layers are clearly visualized on the dispersion curves. A clear increase of spatial amplification is notice around the the position x_{14} or x_{16}, depending on the cases. As visualized, the second shear layer is most unstable than the first one.

However, the amplification levels are similar to the ones found for the P80 cases (cf. Figure 7) and the e^n term, plotted in Figure 11, even is the slightly higher than for the P80, are still of the same order of magnitude.

Then, with the same reason than for the P80, this stability analysis enables to say that there is no risk, at least in this part of the firing, to trigger vortex shedding angle in the P120C.

5. Conclusions

Linear stability analysis enables to clarify a little bit more the scenario leading to the pressure oscillations phenomena present on the last part of the first half of the firing of the P80 and by analogy of the P120C.

The tool developed by Lacassagne[19] is then used with P80 and P120C velocity profiles, extracted from the CFD simulations at several operating times. The comparison with the academic results obtained in Lacassagne[19] shows that the amplification levels of the instability are very small compared to the one of an academic stable shear layer. Moreover the most unstable frequencies are far from longitudinal frequency mode, which do not promote the acoustic coupling needed to trigger pressure oscillations.

Therefore, during theses pressure oscillation occurrences the VSA is not present and can be discarded. This result is in agreement with another AGS works, not described here, in which theses pressures oscillations are explained by the aluminium combustion instability called ITHAC[12] .

This work also shows the efficiency of the local linear stability method to analyse without costly simulations the hydrodynamics instabilities even in real motors configurations.

6. Acknowledgments

References

[1] Esam M Abu-Irshaid, Joseph Majdalani, and G. Casalis. Hydrodynamic stability of rockets with headwall injection. *Physics of Fluids*, 19(2):024101, 2007.

[2] Claudio Canuto. *Spectral Methods in Fluid Dynamics*. Springer Verlag, 1988.

[3] G. Casalis, G. Avalon, and Jean-Philippe Pineau. Spatial instability of planar channel flow with fluid injection through porous walls. *Physics of Fluids*, 10(1):2558–2568, October 1998.

[4] E Cavallini, B Favini, and A Neri. Analysis of Pressure Oscillation during Ignition Transient and Steady-State of an Overloaded VEGA First Stage. 2014.

[5] F Chedevergne, G. Casalis, and Th Féraille. Biglobal linear stability analysis of the flow induced by wall injection. *Physics of Fluids*, 18(1):014103, 2006.

[6] P G Drazin and W H Reid. *Hydrodynamic Stability*. Cambridge University Press, August 2004.

[7] J. Dupays. *Contribution à l'étude du rôle de la phase condensée dans la stabilité d'un propulseur à propegol solide pour lanceur spatial*. PhD thesis, ONERA, October 1996.

[8] J. Dupays, M. Prévost, P. Tarrin, and F Vuillot. Effects of particulate phase on vortex shedding driven oscillations in solid rocket motors. *AIAA 32nd Joint Propulsion Conference*, 1996.

[9] Y. Fabignon, J. Dupays, G. Avalon, F Vuillot, N. Lupoglazoff, G. Casalis, and M. Prévost. Instabilities and pressure oscillations in solid rocket motors. *Aerospace Science and Technology*, 7(3):191–200, April 2003.

[10] M Fiorillo, F Giliberti, and M Angelone. VEGA Solid Rocket Motors Flight Performances results. 2013.

[11] S. Gallier and F. Godfroy. Aluminum Combustion Driven Instabilities in Solid Rocket Motors. *Journal of propulsion and power*, 25(2):509–521, March 2009.

[12] S. Gallier, Emmanuel Radenac, and F. Godfroy. Thermoacoustic Instabilities in Solid Rocket Motors. In *45th AIAA/ASME/SAE/ASEE Joint Propulsion Conference & Exhibit*, Reston, Virigina, August 2009. American Institute of Aeronautics and Astronautics.

[13] S. Gallier, Fabien Sibe, and Olivier Orlandi. Combustion response of an aluminum droplet burning in air. *Proceedings of the Combustion Institute*, 33(2):1949–1956, 2011.

[14] Jérôme Griffond and G. Casalis. On the nonparallel stability of the injection induced two-dimensional Taylor flow. *Physics of Fluids*, 13(6):1635, 2001.

[15] Jérôme Griffond, G. Casalis, and Jean-Philippe Pineau. Spatial instability of flow in a semiinfinite cylinder with fluid injection through its porous walls. *European Journal of Mechanics - B/Fluids*, 19(1):69–87, September 2000.

[16] P Huerre and P A Monkewitz. Absolute and convective instabilities in free shear layers. *Journal of Fluid Mechanics*, 1985.

[17] Matthew P Juniper. Absolute and convective instability in gas turbine fuel injectors. pages 1–10, February 2012.

[18] W Koch. Local instability characteristics and frequency determination of self-excited wake flows. *Journal of Sound and Vibration*, 99(1):53–83, March 1985.

[19] Laura Lacassagne. *Simulations et analyses de stabilité linéaire du détachement tourbillonnaire d'angle dans les moteurs à propergol solide.* . PhD thesis, Institut National Polytechnique de Toulouse, April 2017.

[20] Laura Lacassagne, Thibault Bridel-Bertomeu, E riber, B Cuenot, G. Casalis, and F Nicoud. Lateral blowing impact on corner vortex shedding in solid rocket motors. In *Space Propulsion 2016*, pages 1–11, May 2016.

[21] N. Lupoglazoff, François Vuillot, J. Dupays, and Y. Fabignon. Numerical simulations of the unsteady flow inside segmented solid-propellant motors with burning aluminum particles. In *40th AIAA Aerospace Sciences Meeting & Exhibit*, Reston, Virigina, 2002. American Institute of Aeronautics and Astronautics.

[22] A Michalke. On spatially growing disturbances in an inviscid shear layer. *Journal of Fluid Mechanics*, 1965.

[23] A Michalke. The instability of free shear layers. *Progress in Aerospace Sciences*, 12 IS -:213–216, 1972.

[24] A Neri, S Bianchi, P Pascal, and M Cutroni. An Overview of Vega Solid Rocket Motors Development and Qualification Program. 2003.

[25] K Oberleithner, M SIEBER, C N NAYERI, C O Paschereit, C PETZ, H C HEGE, B R NOACK, and I Wygnanski. Three-dimensional coherent structures in a swirling jet undergoing vortex breakdown: stability analysis and empirical mode construction. *Journal of Fluid Mechanics*, 679:383–414, May 2011.

[26] J Traineau, M. Prévost, F Vuillot, P Le Breton, J Cuny, N Preioni, R Bec, J Traineau, M. Prévost, F Vuillot, P Le Breton, J Cuny, N Preioni, and R Bec. A subscale test program to assess the vortex shedding driven instabilities in segmented solid rocket motors. In *33rd Joint Propulsion Conference and Exhibit*, Reston, Virigina, January 1997. American Institute of Aeronautics and Astronautics.

[27] B Ugurtas, G. Avalon, N. Lupoglazoff, and F Vuillot. Stability and acoustic resonance of internal flows generated by side injection. *Progress in astronautics and aeronautics*, 2000.

[28] François Vuillot. Vortex-shedding phenomena in solid rocket motors. *Journal of propulsion and power*, 11(4):626–639, July 1995.